




The Physical Properties and Starspot Activity of the Triple System KIC 6525196

Yang Pan¹ , Jian-Ning Fu², Xiao-Bin Zhang³, Jia-Xin Wang⁴, and Chun-Qian Li^{3,5}

¹ School of Physics and Astronomy, China West Normal University, Nanchong 637002, China; pyncxh@126.com

² Department of Astronomy, Beijing Normal University, Beijing 100875, China

³ Key Laboratory of Optical Astronomy, National Astronomical Observatories, Chinese Academy of Sciences, Beijing 100012, China

⁴ School of Science, Chongqing University of Posts and Telecommunications, Chongqing 400065, China

⁵ School of Astronomy and Space Science, University of Chinese Academy of Sciences, Beijing 100049, China

Received 2022 April 12; revised 2022 May 15; accepted 2022 May 16; published 2022 June 17

Abstract

We present the results of photometric and spectroscopic analyses for the triple-lined system KIC 6525196, an eclipsing binary accompanied by a third star. By modeling the Kepler light curves and radial velocities from LAMOST and HIDES observations, absolute parameters of the system are determined. Both components of the eclipsing binary are found to be solar-like stars with masses and radii of $M_1 = 1.0286 \pm 0.0026 M_\odot$, $R_1 = 1.127 \pm 0.008 R_\odot$, and $M_2 = 0.9667 \pm 0.0024 M_\odot$, $R_2 = 0.963 \pm 0.007 R_\odot$. The mass of the third star is determined to be $M_3 = 0.772 \pm 0.010 M_\odot$. With the out-of-eclipse light residuals, we measure rotation period and decay timescale of an active region by using the autocorrelation function. In comparison to the Sun, the activity level of the system is significantly stronger. In addition, a possible short photometric activity cycle of ~ 244 days is detected.

Key words: stars: activity – (stars:) binaries: eclipsing – (stars:) binaries: spectroscopic

1. Introduction

The majority of stars are binaries, triples and multiples in galaxies. Recently, eclipse timing variation studies showed that about 20% of close binaries have tertiary companions (Rappaport et al. 2013; Conroy et al. 2014). The masses and orbital parameters of the constituent stars are crucial to understanding the process of the formation and dynamical evolution of triple stars (Toonen et al. 2020). Eclipsing binaries (EBs) are valuable objects because masses and radii can be determined directly from observations, which is important to constrain stellar evolutionary models. In addition, the late-type EBs are also crucial to starspot activities. The properties of starspots, including sizes, decay timescale, and starspot activity cycles, can be deduced from brightness variations due to starspots. For instance, Wang et al. (2022) studied the properties and evolution of starspots on three double-lined detached EBs. Pi et al. (2019) found a ~ 3.6 yr starspot cycle on the RS CVn-type binary DV Psc. Hu et al. (2020) detected a ~ 11 yr magnetic-activity cycle on W UMa-type binary v0599 Aur. Reinhold et al. (2017) found evidence of photometric activity cycles for 3203 Kepler stars by measuring variations of light curve amplitude. Montet et al. (2017) detected a sample of stars with photometric complete cycles from Kepler light curves. Since the masses and orbital properties of the triple stars can be directly measured from the combination of photometry and radial velocities (RVs), triple-lined stars, EBs

plus a tertiary component, are optimal samples for investigating dynamical evolution and stellar activity.

The primary aim of the Kepler mission is to detect transiting exoplanets (Borucki et al. 2010). As a by-product, more than 2000 EBs with continuous high-precision photometry have been discovered (Kirk et al. 2016). The follow-up LAMOST spectroscopic observations in the Kepler field, such as the low-resolution LAMOST-Kepler (LK) project (De Cat et al. 2015; Zong et al. 2018b; Fu et al. 2020) and the time-domain LAMOST-Kepler Medium Resolution Spectroscopic Survey (LK-MRS; Zong et al. 2020), provide reliable atmospheric parameters and RVs for these EBs. By combing LAMOST spectra and photometric light curves, several works of orbital parameters and magnetic activity of EBs have been studied (e.g., Lu et al. 2020; Pan et al. 2020; Zhu et al. 2021; Niu et al. 2022). Therefore, the combination between Kepler photometry and LAMOST spectroscopy gives an opportunity to measure physical parameters and explore starspot activity of triple-lined systems.

KIC 6525196 is a triple-star candidate, a close double-lined EB with a tertiary companion, identified by Rappaport et al. (2013) and Borkovits et al. (2016) via analysis of eclipse time variations (ETV, $P_{\text{ETV}} = 415.8$ days). Later, through an analysis of Kepler light curves in combination with RVs measured from the High-Dispersion Echelle Spectrograph (HIDES) spectrograph, Helminiak et al. (2017) confirmed that KIC 6525196 is a triple-lined spectroscopic system composed

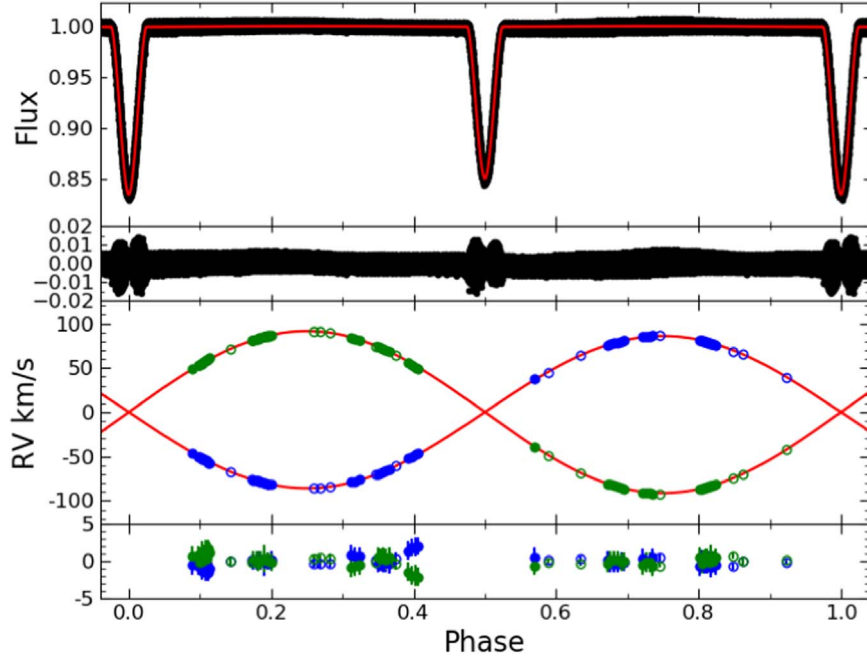


Figure 1. Top: Observed (black dots) and fitted (red line) light curves of KIC 6525196 and the residuals. Bottom: The primary (blue circles) and secondary (green circles) RVs and the corresponding fitting curves (red lines) of KIC 6525196 and the residuals. Filled circles represent RVs from LAMOST, and open ones are the HIDES RVs.

of an inner solar-like double-lined EB and an outer tertiary companion. By convention, the inner double-lined EB is designated as A (=Aa+Ab, namely the primary + the secondary), and the outer tertiary companion as B. In addition, Hełminiak et al. (2017) point out that out-of-eclipse variation of the binary is due to starspot evolution. From the out-of-eclipse variation, two rotation periods ($P_1 \approx 3.392$ days, $P_2 \approx 3.448$ days), close to the orbital period of Aa+Ab ($P_{\text{orb}} \sim 3.420$ days), were identified by Lurie et al. (2017), which hint that there may be two active regions on the binary. To better understand their modulation behavior, an analysis of out-of-eclipse variation is needed.

This paper is organized as follows. In Section 2, we describe the Kepler photometric and LAMOST spectroscopic observations, and the determination of RVs. In Section 3, the inner-orbit modeling and outer-orbit modeling are carried out to determine the physical parameters of KIC 6525916. Section 4 presents the analysis of the out-of-eclipse residuals and the analysis results are discussed in Section 5, finally followed by a summary in Section 6.

2. Kepler Photometry and LAMOST Spectroscopy

KIC 6525196 was observed by Kepler in long-cadence mode (29.4 minutes sampling) and short-cadence mode (59 s sampling). There are 18 long-cadence quarters of data (Q0–Q17) and two short-cadence quarters of data (Q2, Q3). The

contamination factors reported in MAST⁶ are lower, $4.0e-4$, in all long-cadence quarters, which indicates that the photometry of the targets there is hardly contaminated by light from nearby stars. In this study, we only use the detrended and normalized long-cadence data provided by the Kepler Eclipsing Binary Catalog (KEBC, Prša et al. 2011; Slawson et al. 2011; Kirk et al. 2016). The obvious outliers in the light curves were removed. Using the linear ephemerids given by the KEBC, the phase-folded long-cadence light curves are displayed in the top panel of Figure 1.

KIC 6525196 was observed by the LK-project in low-resolution mode and the LK-MRS survey in medium-resolution mode. The combination of the two observation modes can be beneficial. In the low-resolution mode, the atmospheric parameters can be determined easily. However, we cannot distinguish the contribution of the primary, secondary and a possible third components of the triple system. But, in the medium-resolution mode, it is easy to distinguish the spectra of the primary and secondary components of some detached EBs, such as 2MASS J04100497+2931023 (Meng et al. 2021). In addition, the LAMOST spectra are helpful to the study of magnetic activity (e.g., Zhang et al. 2020, 2021b). Two low-resolution spectra (wavelength range 370–900 nm, $R \sim 1800$) with signal-to-noise ratio (S/N) ~ 100 and seventy-one medium-resolution ones (wavelength range 495–535 nm and

⁶ https://archive.stsci.edu/kepler/data_search/search.php

630–680 nm, $R \sim 7500$) with S/N greater than 30 were obtained. The atmospheric parameters from the low-resolution spectrum are given in LAMOST Data Release 8 (DR8)⁷ as $T_{\text{eff}} = 6103 \pm 22$ K, $\log g = 4.28 \pm 0.04$, $[\text{Fe}/\text{H}] = -0.53 \pm 0.02$. With the medium-resolution spectra, we extracted RVs by a cross-correlation algorithm (Li et al. 2021). Twenty single-lined RVs (v_1), fifteen double-lined RVs (v_1, v_2) and thirty-six triple-lined RVs (v_1, v_2, v_3) were extracted. The subscripts 1, 2 and 3 respectively refer to the primary (Aa), the secondary (Ab) and the tertiary companion (B). In the following analysis, only the double-lined and triple-lined RVs are considered. To correct the RV variations (v_1, v_2) of the close binary caused by the third star, the systemic velocities (γ) of the binary were calculated as the formula described in Helminiak et al. (2017)

$$\gamma(t_i) = \frac{v_1(t_i) + qv_2(t_i)}{1 + q}, \quad (1)$$

where q is mass ratio, and $v_1(t_i)$ and $v_2(t_i)$ are the RVs of the binary at any time t_i . Adopting the value of mass ratio (0.9383) given in Table 2 in Helminiak et al. (2017), the corrected RVs of the binary ($v_1(t_i) - \gamma(t_i)$, $v_2(t_i) - \gamma(t_i)$) are shown in Figure 1. Further, since there exists zero-point offset among RVs (Liu et al. 2019; Zhang et al. 2021a), the RVs of the third star are calibrated by the APOGEE RV standard stars published in Huang et al. (2018). The calibrated RVs of the third components (v_3) are presented in Table 1 and are displayed in Figure 1. Meanwhile, the HIDES RVs corresponding to the close binary and the third star from Helminiak et al. (2017) are also listed in Table 1 and displayed in Figure 1.

3. The Inner-orbit and Outer-orbit Modeling

The triple-lined system KIC 6525196 consists of the inner EB Aa+Ab and the outer companion B. Under the assumption that the inner-orbit of Aa+Ab is Keplerian and circular, to obtain physical parameters of inner pair Aa+Ab, we simultaneously modeled a phase-binned average light curve and RVs using the Wilson–Devinney (WD, 2013) code (Wilson & Devinney 1971; Wilson 1979, 1990, 2012).

We adopt the effective temperature of the primary to be $T_1 = 6103$ K determined from the LAMOST low-resolution spectrum at the nearby conjunction phase. The gravity-darkening exponents and bolometric albedos for each star with convective envelopes (Lucy 1967; Ruciński 1969) were set to be 0.5 and 0.32, respectively. The logarithmic monochromatic limb-darkening coefficients in Kepler band (x_K, y_K) were interpolated from WD code, and the logarithmic bolometric ($X_{\text{bolo}}, Y_{\text{bolo}}$) ones were adopted from van Hamme (1993). The ten adjustable parameters in the model are the inclination (i), the mass ratio ($q = m_2/m_1$), the semimajor axis of the binary (a), the center-of-mass velocity (γ_0), the effective temperature

of the secondary (T_2), the surface potential ($\Omega_{1,2}$), the phase shift, the dimensionless luminosity of the primary (L_1) and the third light (l_3).

Table 2 gives the orbital and physical parameters of the best-fit model. Since the errors of the fitting parameters in the WD code are only fitting errors and are underestimated (Prša & Zwitter 2005), the errors of the absolute parameters are also underestimated. Figure 1 shows the synthetic light curves and RVs (red lines) from the best-fit model as well as the observed minus computed ($O - C$) residuals. The results suggest that the close binary consists of two solar-like stars which are consistent with the ones in Table 2 in Helminiak et al. (2017).

The system parameters of outer orbit A+B have been determined from ETVs (Rappaport et al. 2013; Borkovits et al. 2016) and HIDES RVs (Helminiak et al. 2017). With the HIDES RVs and supplemental RVs from LAMOST, as depicted in Figure 2, we recalculate the system parameters of the outer orbit. Since the distance between A and B is much larger than the semimajor axis of the close binary, the A+B pair can be assumed as a binary in a Keplerian orbit. The free parameters are orbital period (P_{AB}), pericenter time (T_{per}), semi-amplitudes (K_A, K_B), eccentricity (e_{AB}), systemic velocity of the whole triple (γ_{AB}) and longitude of periastron (ω_{AB}). These RVs are fitted with the EMCEE code.⁸ The criteria for convergence are that the length of sample chains must be greater than 100 times the estimated autocorrelation time (Goodman & Weare 2010) and such relative variations must be by less than 5%. The results are listed in Table 3 and are in agreement with parameters obtained by Helminiak et al. (2017). Figure 2 shows the systemic velocities of the close binary (Aa+Ab) and the directly measured RVs of the third component. Since the absolute mass of A ($M_A = M_1 + M_2$) has been determined from the inner-orbit modeling (see Table 2), the inclination of the outer orbit could be calculated to be $i_{\text{AB}} \sim 85^\circ$, and then the mass of the third star (M_B , namely M_3) is determined to be $M_B \sim 0.77 M_\odot$.

4. Analysis of Out-of-eclipse Flux Residuals

The out-of-eclipse flux residuals are obtained by subtracting the fitted light curves from the detrended data. The top panel of Figure 3 shows the out-of-eclipse variations due to starspot modulation from Q1-17, together with zoom-in views from Q4 in the middle panel. To study the behaviors of the starspot modulation, using the out-of-eclipse residuals, we measure rotation period, decay timescale, and size of active region and detect photometric activity cycle.

⁷ <http://www.lamost.org/dr8/v1.0/>

⁸ <https://emcee.readthedocs.io/en/stable/>

Table 1
KIC 6525196 Radial Velocities

Time (BJD-2,450,000)	Phase _{Aa+Ab} (Phase ^a)	Phase _{A+B} (Phase ^b)	V_1 (km s ⁻¹)	V_2 (km s ⁻¹)	V_3 (km s ⁻¹)	γ (km s ⁻¹)	Source	S/N
8263.27405	0.3501	0.6264	-70.30 ± 1.20	73.90 ± 1.30	15.70 ± 1.60	-0.50 ± 1.77	LAMOST	97
8263.28725	0.3540	0.6265	-69.20 ± 1.20	72.10 ± 1.30	17.10 ± 1.50	-0.80 ± 1.77	LAMOST	103
8263.29974	0.3576	0.6265	-67.60 ± 1.20	71.50 ± 1.30	15.10 ± 1.60	-0.26 ± 1.77	LAMOST	100
8263.31294	0.3615	0.6265	-66.10 ± 1.30	69.80 ± 1.40	16.10 ± 1.80	-0.31 ± 1.91	LAMOST	75
8263.32544	0.3652	0.6266	-65.80 ± 1.30	68.00 ± 1.30	15.10 ± 1.70	-1.03 ± 1.84	LAMOST	85
8267.23046	0.5068	0.6359	-4.40 ± 1.20				LAMOST	99
8267.24296	0.5104	0.6359	-4.40 ± 1.20				LAMOST	98
8267.25616	0.5143	0.6360	-3.30 ± 1.20				LAMOST	113
8267.26866	0.5179	0.6360	-2.60 ± 1.20				LAMOST	113
8267.28116	0.5216	0.6360	0.00 ± 1.30				LAMOST	121
8267.29435	0.5254	0.6360	4.90 ± 1.40				LAMOST	110
8267.31449	0.5313	0.6361	11.00 ± 1.20				LAMOST	127
8268.23814	0.8014	0.6383	80.71 ± 1.30	-86.25 ± 1.30	16.28 ± 1.60	-0.11 ± 1.84	LAMOST	86
8268.24786	0.8042	0.6383	80.67 ± 1.30	-87.11 ± 1.30	17.80 ± 1.70	-0.55 ± 1.84	LAMOST	96
8268.25689	0.8068	0.6383	79.72 ± 1.30	-85.93 ± 1.40	17.83 ± 1.70	-0.47 ± 1.91	LAMOST	85
8268.26592	0.8095	0.6384	79.29 ± 1.30	-85.27 ± 1.40	18.04 ± 1.70	-0.37 ± 1.91	LAMOST	84
8268.27564	0.8123	0.6384	78.72 ± 1.30	-84.60 ± 1.40	17.59 ± 1.80	-0.34 ± 1.91	LAMOST	80
8268.28536	0.8152	0.6384	78.77 ± 1.30	-84.04 ± 1.30	17.29 ± 1.70	-0.04 ± 1.84	LAMOST	87
8268.29439	0.8178	0.6384	77.52 ± 1.40	-82.46 ± 1.50	18.18 ± 1.70	0.08 ± 2.05	LAMOST	63
8268.30620	0.8213	0.6385	77.23 ± 1.30	-82.36 ± 1.30	15.48 ± 1.60	-0.03 ± 1.84	LAMOST	88
8268.31592	0.8241	0.6385	76.40 ± 1.30	-81.06 ± 1.30	17.25 ± 1.70	0.17 ± 1.84	LAMOST	82
8269.25554	0.0988	0.6407	-51.52 ± 1.20	51.32 ± 1.30		-1.74 ± 1.77	LAMOST	116
8269.26874	0.1027	0.6408	-53.72 ± 1.20	52.89 ± 1.30		-2.11 ± 1.77	LAMOST	119
8269.28193	0.1065	0.6408	-55.41 ± 1.20	55.70 ± 1.30		-1.62 ± 1.77	LAMOST	119
8269.29443	0.1102	0.6408	-56.57 ± 1.30	57.28 ± 1.50		-1.46 ± 1.98	LAMOST	79
8269.30763	0.1140	0.6409	-58.73 ± 1.20	59.98 ± 1.30		-1.27 ± 1.77	LAMOST	116
8270.25975	0.3924	0.6431	-54.01 ± 1.20	54.12 ± 1.30		-1.67 ± 1.77	LAMOST	132
8270.27572	0.3970	0.6432	-52.29 ± 1.20	50.76 ± 1.30		-2.4 ± 1.77	LAMOST	135
8270.29239	0.4019	0.6432	-50.18 ± 1.20	48.44 ± 1.40		-2.44 ± 1.84	LAMOST	104
8270.30836	0.4066	0.6433	-47.99 ± 1.20	46.09 ± 1.30		-2.45 ± 1.77	LAMOST	137
8625.27738	0.1804	0.4921	-73.80 ± 1.20	86.50 ± 1.20	6.40 ± 1.50	3.80 ± 1.70	LAMOST	110
8625.29335	0.1850	0.4921	-74.70 ± 1.20	88.20 ± 1.20	5.30 ± 1.50	4.16 ± 1.70	LAMOST	117
8625.31002	0.1899	0.4921	-76.10 ± 1.80	89.20 ± 1.80	6.00 ± 2.10	3.92 ± 2.55	LAMOST	33
8644.23159	0.7215	0.5374	88.50 ± 1.30	-86.80 ± 1.30	10.40 ± 1.60	3.64 ± 1.84	LAMOST	109
8644.24826	0.7264	0.5374	88.30 ± 1.20	-87.20 ± 1.30	10.40 ± 1.40	3.34 ± 1.77	LAMOST	115
8644.26423	0.7311	0.5375	88.60 ± 1.20	-87.60 ± 1.30	10.20 ± 1.40	3.30 ± 1.77	LAMOST	123
8644.28090	0.736	0.5375	88.90 ± 1.20	-89.00 ± 1.20	9.20 ± 1.50	2.78 ± 1.70	LAMOST	118
8646.25110	0.3119	0.5422	-76.60 ± 1.30	85.70 ± 1.30	10.70 ± 1.70	1.97 ± 1.84	LAMOST	87
8646.26777	0.3168	0.5422	-75.80 ± 1.20	84.80 ± 1.30	11.10 ± 1.50	1.94 ± 1.77	LAMOST	112
8646.29000	0.3233	0.5423	-75.00 ± 1.20	82.60 ± 1.20	10.80 ± 1.60	1.29 ± 1.70	LAMOST	97
9001.23198	0.0892	0.3910	-37.70 ± 1.30	57.70 ± 1.30		8.48 ± 1.84	LAMOST	95
9001.25976	0.0973	0.3911	-42.10 ± 1.20	61.20 ± 1.20		7.91 ± 1.70	LAMOST	176
9001.27781	0.1026	0.3911	-45.40 ± 1.20	63.80 ± 1.20		7.46 ± 1.70	LAMOST	166
9001.29379	0.1073	0.3912	-47.70 ± 1.20	66.00 ± 1.20		7.34 ± 1.70	LAMOST	133
9001.31045	0.1121	0.3912	-49.90 ± 1.30	68.00 ± 1.30		7.17 ± 1.84	LAMOST	87
9003.22580	0.6721	0.3958	84.60 ± 1.20	-72.40 ± 1.20	-2.90 ± 1.50	8.60 ± 1.70	LAMOST	118
9003.24178	0.6767	0.3958	85.30 ± 1.20	-73.00 ± 1.20	-3.20 ± 1.40	8.67 ± 1.70	LAMOST	132
9003.25775	0.6814	0.3959	86.40 ± 1.20	-74.30 ± 1.20	-3.80 ± 1.40	8.61 ± 1.70	LAMOST	137
9003.27442	0.6863	0.3959	87.20 ± 1.20	-75.60 ± 1.20	-3.70 ± 1.30	8.39 ± 1.70	LAMOST	143
9003.29039	0.6910	0.3960	88.30 ± 1.20	-77.10 ± 1.20	-3.90 ± 1.30	8.23 ± 1.70	LAMOST	145
9003.30636	0.6956	0.3960	88.60 ± 1.20	-78.30 ± 1.20	-3.90 ± 1.40	7.81 ± 1.70	LAMOST	146
9004.24390	0.9697	0.3982	0.40 ± 1.30				LAMOST	155
9004.25987	0.9744	0.3983	3.20 ± 1.20				LAMOST	163
9004.27584	0.9790	0.3983	3.80 ± 1.20				LAMOST	160
9004.29251	0.9839	0.3984	4.30 ± 1.10				LAMOST	152
9004.30848	0.9886	0.3984	4.30 ± 1.10				LAMOST	137
9006.29745	0.5701	0.4032	46.10 ± 1.20	-30.70 ± 1.20		8.92 ± 1.70	LAMOST	172
9011.26151	0.0213	0.4150	2.60 ± 1.20				LAMOST	109

Table 1
(Continued)

Time (BJD-2,450,000)	Phase _{Aa+Ab} (Phase ^a)	Phase _{A+B} (Phase ^b)	V_1 (km s ⁻¹)	V_2 (km s ⁻¹)	V_3 (km s ⁻¹)	γ (km s ⁻¹)	Source	S/N
8263.27405	0.3501	0.6264	-70.30 ± 1.20	73.90 ± 1.30	15.70 ± 1.60	-0.50 ± 1.77	LAMOST	97
9011.27818	0.0262	0.4151	-0.50 ± 1.30				LAMOST	113
9011.29415	0.0308	0.4151	-5.20 ± 1.40				LAMOST	89
9011.31082	0.0357	0.4151	-9.90 ± 1.30				LAMOST	85
9015.20539	0.1743	0.4245	-69.70 ± 1.10	88.20 ± 1.20	-0.30 ± 1.30	6.74 ± 1.63	LAMOST	175
9015.22136	0.1789	0.4245	-70.90 ± 1.10	89.20 ± 1.20	-0.60 ± 1.30	6.60 ± 1.63	LAMOST	188
9015.23803	0.1838	0.4245	-72.00 ± 1.10	89.80 ± 1.10	-0.60 ± 1.30	6.32 ± 1.56	LAMOST	193
9015.26095	0.1905	0.4246	-73.90 ± 1.10	91.40 ± 1.10	-1.00 ± 1.30	6.12 ± 1.56	LAMOST	185
9015.27762	0.1954	0.4246	-74.80 ± 1.10	92.00 ± 1.20	-1.50 ± 1.30	5.95 ± 1.63	LAMOST	198
9015.29359	0.2000	0.4247	-76.00 ± 1.10	92.30 ± 1.20	-1.50 ± 1.30	5.47 ± 1.63	LAMOST	183
9016.24917	0.4794	0.4269	3.00 ± 1.10				LAMOST	131
9016.26515	0.4841	0.4270	3.50 ± 1.10				LAMOST	128
9016.28112	0.4887	0.4270	3.80 ± 1.10				LAMOST	129
9016.29779	0.4936	0.4271	3.60 ± 1.10				LAMOST	126
6865.06230	0.5885	0.283	58.51 ± 0.23	-35.42 ± 0.31		13.02 ± 0.22	HIDES	54
6865.22093	0.6349	0.2834	77.45 ± 0.35	-56.07 ± 0.4	-16.54 ± 0.05	12.79 ± 0.3	HIDES	66
6866.00078	0.8629	0.2853	77.89 ± 0.36	-56.71 ± 0.44	-16.41 ± 0.07	12.70 ± 0.32	HIDES	43
6867.06159	0.1730	0.2878	-63.31 ± 0.38	93.42 ± 0.25	-16.16 ± 0.06	12.60 ± 0.28	HIDES	41
6912.12629	0.3475	0.3956	-62.02 ± 0.32	82.64 ± 0.35	-4.59 ± 0.07	8.04 ± 0.28	HIDES	62
6914.09569	0.9232	0.4003	47.41 ± 0.30	-34.44 ± 0.22	-3.89 ± 0.06	7.77 ± 0.20	HIDES	49
7062.36232	0.2684	0.7548	-90.94 ± 0.60	86.07 ± 0.38	30.93 ± 0.08	-5.21 ± 0.41	HIDES	44
7112.23530	0.8485	0.8741	63.36 ± 0.38	-79.61 ± 0.39	32.0 ± 0.06	-5.88 ± 0.31	HIDES	73
7144.20856	0.1958	0.9505	-81.87 ± 0.39	85.91 ± 0.63	17.55 ± 0.06	-0.61 ± 0.41	HIDES	40
7148.23852	0.3739	0.9602	-60.16 ± 0.72	65.22 ± 0.68	14.51 ± 0.04	0.56 ± 0.52	HIDES	39
7294.93288	0.2594	0.3109	-74.30 ± 0.41	103.45 ± 0.38	-13.69 ± 0.07	11.78 ± 0.34	HIDES	50
7297.95686	0.1435	0.3182	-56.30 ± 0.38	82.87 ± 0.60	-12.57 ± 0.1	11.1 ± 0.38	HIDES	48
7529.19525	0.7451	0.8711	80.21 ± 0.47	-98.13 ± 0.27	32.32 ± 0.05	-6.16 ± 0.33	HIDES	63
7541.29669	0.2829	0.9000	-89.39 ± 0.56	84.86 ± 0.62	28.97 ± 0.07	-5.00 ± 0.46	HIDES	45

Notes.^a Relative to T_0 at the primary eclipse.^b Relative to $T_{\text{per}} = 2456746.7$ days. The subscripts 1, 2 and 3 represent the primary (Aa), secondary (Ab) and tertiary (B), respectively.

4.1. The Rotation Period, Decay Timescale and Size of Active Region

The rotation period and decay timescale of an active region are measured using the discrete autocorrelation function (ACF) method (Edelson & Krolik 1988; McQuillan et al. 2013, 2014; Giles et al. 2017). The ACF calculates the degree of self-similarity of light curves at a series of different time lags. The ACF of the out-of-eclipse residuals for Q1-17 is displayed in the bottom panel of Figure 3. Due to starspot decay in the active region, the peak in the ACF decreases with the increase of time lag. According to Giles et al. (2017), this behavior is analogous to the displacement of an underdamped simple harmonic oscillator (uSHO),

$$y(t) = e^{-t/\tau_{\text{AR}}} \left(A \cos\left(\frac{2\pi t}{P}\right) + B \cos\left(\frac{4\pi t}{P}\right) + y_0 \right). \quad (2)$$

Here τ_{AR} and P are, respectively, the decay timescale and rotation period of the dominant active region, and A , B and y_0 are fit parameters without significant meaning. To obtain the

decay timescale of the active region, the ACF of the out-of-eclipse residuals is fitted by the uSHO equation (Giles et al. 2017) utilizing the code EMCEE. The fitting results are expressed in Table 4.

Based on Giles et al. (2017), the root mean square (rms) scatter of out-of-eclipse residuals can be regarded as the starspot size, $\text{rms} = \sqrt{\frac{1}{N} \sum_{i=1}^N y_i^2}$, where N and y_i represent the number of data points and their mag value in the residuals, respectively. We calculate the rms for each orbital cycle. The mean value of rms is listed in Table 4.

4.2. The Detection of Photometric Activity Cycle

To describe the time behavior of the out-of-eclipse residuals, a time-frequency analysis called sliding Lomb–Scargle periodogram (sLSP; Zong et al. 2018a) is applied to show the variation of the amplitudes and periods. The sliding window width and time step are set to 90 days and 2 days, respectively. Figure 4 displays the sLSP. The magnitude of the normalized amplitude is indicated by the color bar. From the sLSP

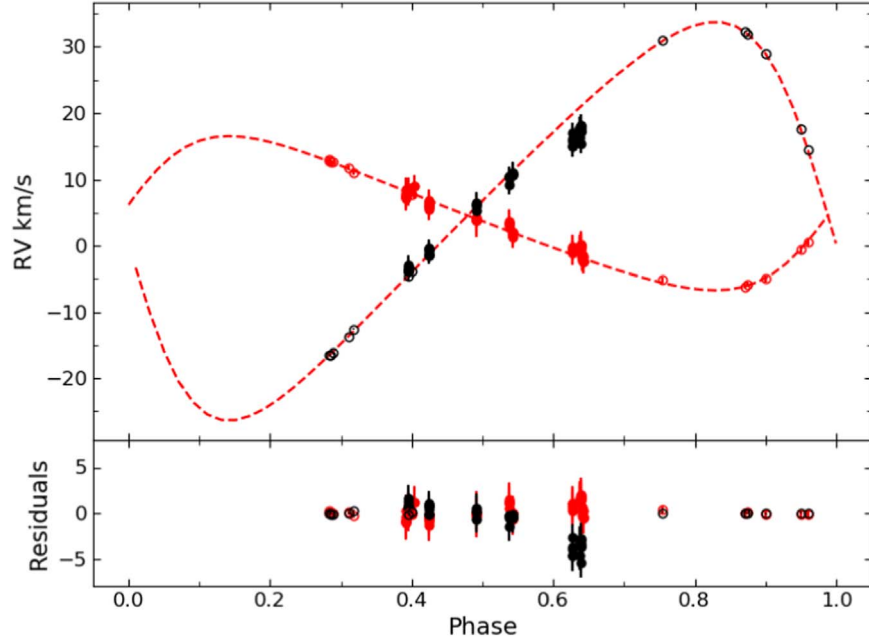


Figure 2. The RVs of the outer orbit A+B. Red circles signify the calculated systemic RVs of the inner binary Aa+Ab (γ), and black circles represent the direct RV measurements of the third component (B) (v_3). Filled circles correspond to RVs from LAMOST, and open ones are RVs from HIDES. The red dashed lines are fitting curves.

Table 2

Physical Parameters of the Inner Binary Aa+Ab

Parameter	Best-fit Value
T_0	$2454954.352139 \pm 0.024179$
e	0.0 (fixed)
ω (deg)	...
P_{orb} (day)	3.4206042 ± 0.0000062
$q = M_2/M_1$	0.939 ± 0.001
i (deg)	85.34 ± 0.01
T_{eff} (K)	6103 (fixed)
T_2 (K)	5950 ± 100^a
T_2/T_1	0.974 ± 0.021
Ω_1	11.61 ± 0.01
Ω_2	12.75 ± 0.01
a (R_\odot)	12.02 ± 0.01
M_1 (M_\odot)	1.0286 ± 0.0026
M_2 (M_\odot)	0.9667 ± 0.0024
R_1 (R_\odot)	1.127 ± 0.008
R_2 (R_\odot)	0.963 ± 0.007
L_1 (L_\odot)	1.592 ± 0.104
L_2 (L_\odot)	1.046 ± 0.070
l_3	0.257 ± 0.002
$\log g_1$ (cgs)	4.35 ± 0.01
$\log g_2$ (cgs)	4.45 ± 0.01

Note.

^a Assumed.

diagram, the normalized amplitudes of the active region have an obvious quasi-periodic modulation with period of ~ 200 days, which hints that a starspot activity cycle probably exists.

Table 3

Physical Parameters of the Outer Orbit System A+B

Parameter	This Work
P_{AB} (day)	418.2 ± 0.2
T_{per} (JD-2,450,000)	6746.7 ± 0.1
K_A (km s^{-1})	11.64 ± 0.15
K_B (km s^{-1})	30.08 ± 0.08
$q = B/A$	0.387 ± 0.005
e_{AB}	0.300 ± 0.002
ω_{AB} (deg)	275.68 ± 0.32
γ_{AB} (km s^{-1})	4.56 ± 0.04
$M_A \sin^3(i_{\text{AB}})(M_\odot)$	1.968 ± 0.018
$M_B \sin^3(i_{\text{AB}})(M_\odot)$	0.761 ± 0.016
$a_{\text{AB}} \sin(i_{\text{AB}})$ (au)	1.528 ± 0.006
i_{AB} (deg)	84.5 ± 1.9
M_A (M_\odot)	$1.9953^a \pm 0.0036$
M_B (M_\odot)	0.7721 ± 0.0102
a_{AB} (au)	1.535 ± 0.008

Note.

^a Directly from Table 2.

According to Reinhold et al. (2017), the amplitudes of the out-of-eclipse light curve residuals can also be used to detect the photometric activity cycle. Therefore, first, we calculate the variability range R_{var} (Basri et al. 2011) in every orbital cycle (E). Then, a Lomb–Scargle (LS) periodogram is computed for the R_{var} . Figure 5 shows the R_{var} evolving with E (top panel) and its LS periodogram (bottom panel). An obvious periodicity ($0.014/E \simeq 244$ days) in the R_{var} can be found in the LS periodogram.

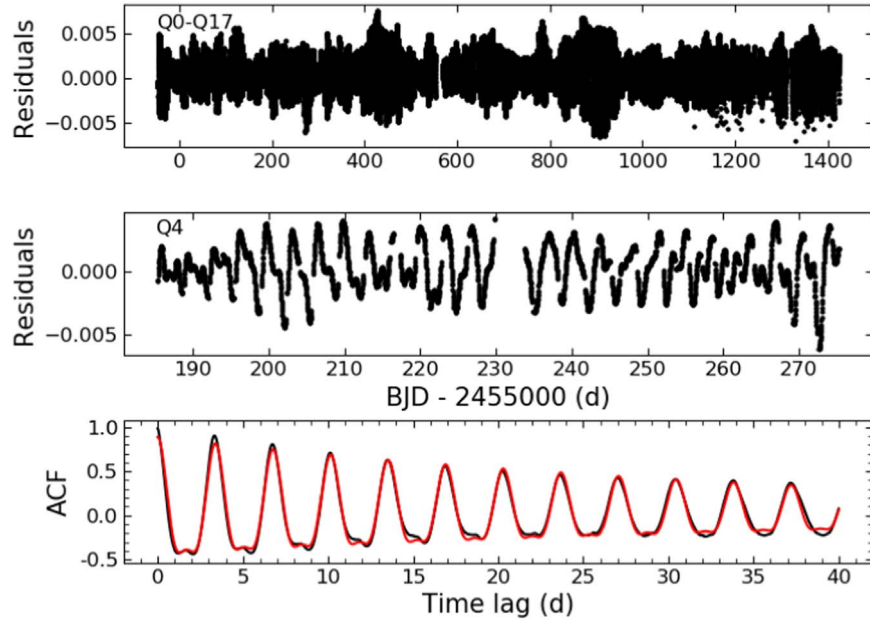


Figure 3. Top and middle panels show the out-of-eclipse flux residuals for Q0-17 and Q4, respectively. Bottom panel displays the ACF (black) of all the out-of-eclipse residuals and the fitted ACF (red) using the uSHO equation.

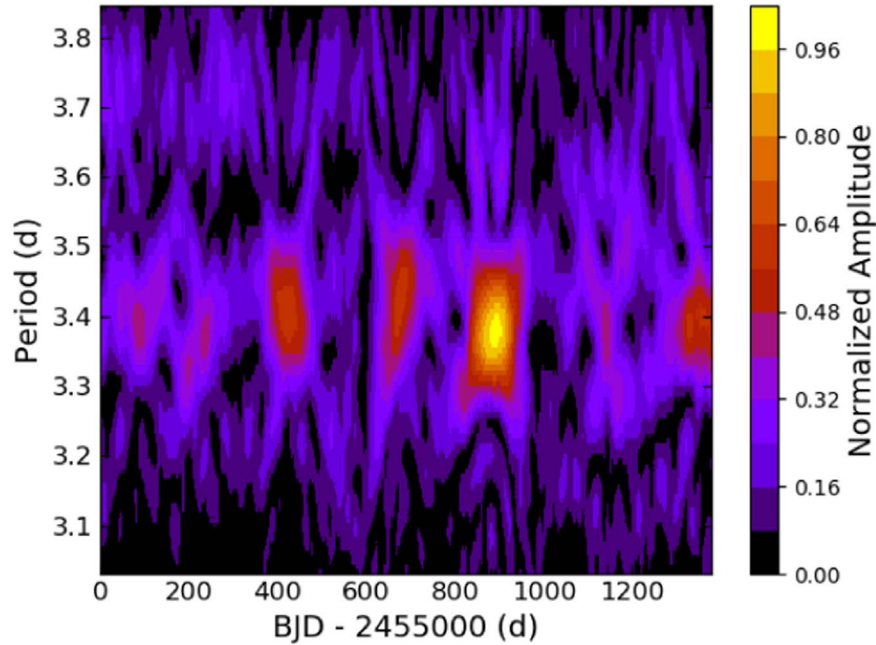


Figure 4. sLSP of the out-of-eclipse residuals. The normalized amplitudes are represented by color as a function of time and period.

Table 4

The rms and Best-fitting Parameters of ACF

rms (mag)	P_{ACF} (day)	τ_{AR} (day)	A	B	y_0
0.002	3.38	32.20	0.67	0.25	0.0172

5. Discussion

The modeling of the inner and outer orbits shows that KIC 6525196 is composed of an F-type EB and a low-mass third star. The inclination of the outer orbit is $\sim 85^\circ$, very close to the result ($\sim 80^\circ$) given by Borkovits et al. (2016). This indicates

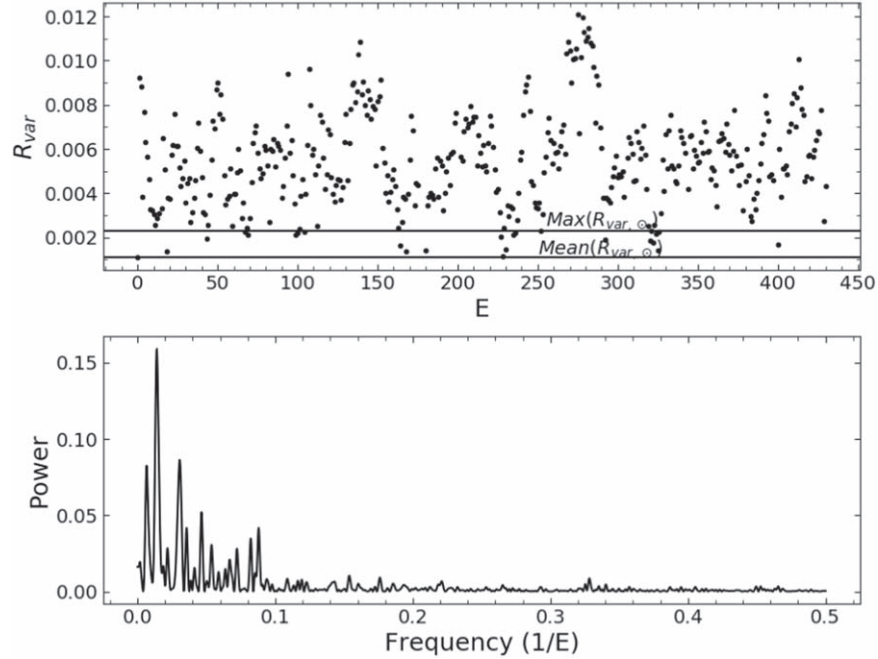


Figure 5. Top: Black points represent the variability range R_{var} in every orbital cycle E for KIC 6525196 and black lines signify the max and mean of R_{var} for the Sun, respectively. Bottom: The LS periodogram of the variability range R_{var} .

that the mutual inclination (i_m) between the inner and outer orbit is small. However, neither tertiary eclipses nor eclipse depth variations were found (Hełminiak et al. 2017). According to Hilditch (2001), the condition for eclipses to be observed is $\sin(90^\circ - i) \leq (R_1 + R_2)/a$, where R_1 , R_2 and a are the radii and separation of stars respectively, and i is orbital inclination. Thus, for the A+B pair, the eclipses caused by the third star can be seen when $R_B \geq a \sin(90^\circ - i_m) - R_A$. Under the assumption that $i_m = 5^\circ$, $R_A = 1.1 R_\odot$ and $a = a_{\text{AB}}$, only when $R_B \geq 27.7 R_\odot$ can the eclipses be seen. Therefore, considering that the triple is a low-mass star, it is considered to be normal in the sense of manifesting no signs of tertiary eclipse.

The ACF panel of Figure 3 shows a very small bulge exists at the half rotation period. Usually, this phenomenon can be explained by two active regions with different strengths on opposite hemispheres (McQuillan et al. 2013; Giles et al. 2017). However, the simulation of starspot distribution and lifetimes (Basri & Shah 2020) demonstrates that random starspot distribution in time and position can also lead to the emergence of peaks with smaller height in the ACF at half the rotation period. Therefore, it is possibly inaccurate to infer the existence of the two active regions or longitudes merely from light curves.

The mean rms of the binary (0.002 mag) is larger than the rms of the Sun, 150 ppm (Morris et al. 2019). In addition, as displayed in the top panel of Figure 5, the R_{var} of the binary is noticeably greater than the Sun at one stage, $\langle R_{\text{var},\odot} \rangle = 0.0011$,

$\max(R_{\text{var},\odot}) = 0.0023$ (Reinhold et al. 2013). This indicates that the rotational variability on the binary is stronger than the one on the Sun and that either the number of starspots is greater than typically found on the Sun or the sizes of the starspots are larger than typical sunspots. Considering that both components (Aa+Ab) are solar-type stars, the reason for the difference in activity level between the binary and the Sun may be a shorter rotation period of the binary than the Sun, and both components could be the source of starspot activity. In addition, the starspots' decay timescale (~ 32 days) on the binary is slightly longer than that of sunspots which have lifetimes of days to a few weeks (Solanki 2003).

A cyclic variation of ~ 244 days is detected from the LS periodogram of R_{var} , which hints that there perhaps exists a short starspot activity cycle with length shorter than 1 yr, similar to Rieger-type cycles on the Sun (McIntosh et al. 2015). However, according to Basri & Shah (2020), short ‘‘activity cycles’’ can be generated by starspot random processes including random bunchings of spot birth dates and the length of the ‘‘activity cycles’’ depends on the ratio between starspot lifetime and stellar rotation. Therefore, additional evidence (for example the color information or Ca II) from other diagnostics is needed to support the interpretation of short activity cycle for the light variation. Pi et al. (2019) found that there exists an obvious linear correlation between $\log(P_{\text{cyc}}/P_{\text{orb}})$ and $\log(1/P_{\text{orb}})$ for short-period EBs with activity cycle. To check whether our results are in accord with the linear correlation, we plot our results ($P_{\text{cyc}} \sim 244$ days,

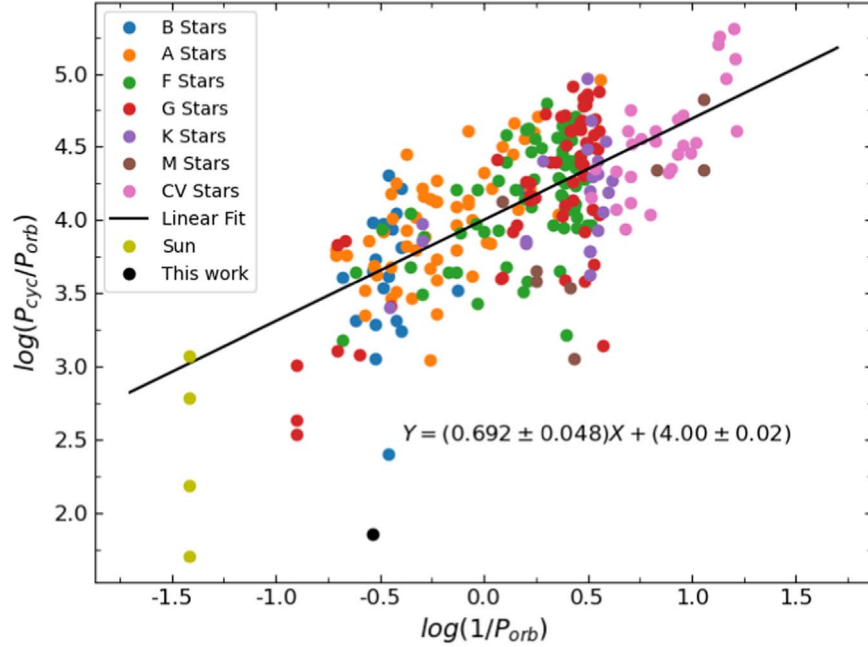


Figure 6. The $\log(P_{\text{cyc}}/P_{\text{orb}})$ vs. $\log(1/P_{\text{orb}})$ for short-period EBs with activity cycle using data given in Table 13 of Pi et al. (2019). Different colors represent different spectral types. CV means cataclysmic variables. The black solid line is a linear fit.

$P_{\text{orb}} \sim 3.42$ days, black point) on Figure 6, with a log–log scale of $P_{\text{cyc}}/P_{\text{orb}}$ versus $1/P_{\text{orb}}$ plot for short-period EBs with cycles and the Sun, using the collected data given in Table 13 of Pi et al. (2019). We refit the data with a linear function. A slope of ~ 0.69 is consistent with the result (~ 0.71) of Pi et al. (2019). As is apparent in Figure 6, the black point deviates from the linear relationship, which indicates that the detected cycle from KIC 6525196 may be just one of many cycles, similar to many EBs and the Sun which have more than one cycle.

6. Summary

The Kepler photometric and LAMOST and HIDES spectroscopic analyses reveal that KIC 6525196 is a triple-lined system consisting of a close EB with a distant low-mass tertiary body and both components (Aa+Ab) in the close binary are solar-like stars. In addition, there is no conflict between the small mutual inclination (i_m) and no signs of tertiary eclipses.

The analysis of out-of-eclipse residuals suggests that there perhaps exists two dominant active regions on opposite hemispheres. Since Aa+Ab have similar properties, both components could be the source of starspot activity. The rotation periods of the active regions are close to the orbital period of the binary. The decay timescale and mean size of the active region are ~ 32 days and 0.002 mag respectively. Compared with the Sun, the activity level is significantly stronger. A possible short spot activity cycle of ~ 244 days is detected from the out-of-eclipse light variation.

Acknowledgments

The Guoshoujing Telescope (the Large Sky Area Multi-Object Fiber Spectroscopic Telescope, LAMOST) is a National Major Scientific Project built by the Chinese Academy of Sciences. Funding for the project has been provided by the National Development and Reform Commission. LAMOST is operated and managed by the National Astronomical Observatories, Chinese Academy of Sciences. This paper includes data collected by the Kepler mission. We acknowledge support from the National Natural Science Foundation of China (NSFC, Grant Nos. 11833002, 12090040, 12090042 and 11973053), support from the Sichuan Youth Science and Technology Innovation Research Team (Grant No. 21CXTD0038), and the Innovation Team Funds of China West Normal University (Grant No. KCXTD2022-6).

ORCID iDs

Yang Pan  <https://orcid.org/0000-0001-8637-5492>

References

- Basri, G., & Shah, R. 2020, *ApJ*, 901, 14
- Basri, G., Walkowicz, L. M., Batalha, N., et al. 2011, *AJ*, 141, 20
- Borkovits, T., Hajdu, T., Sztakovics, J., et al. 2016, *MNRAS*, 455, 4136
- Borucki, W. J., Koch, D., Basri, G., et al. 2010, *Sci*, 327, 977
- Conroy, K. E., Prša, A., Stassun, K. G., et al. 2014, *AJ*, 147, 45
- De Cat, P., Fu, J. N., Ren, A. B., et al. 2015, *ApJS*, 220, 19
- Edelson, R. A., & Krolik, J. H. 1988, *ApJ*, 333, 646
- Fu, J.-N., Cat, P. D., Zong, W., et al. 2020, *RAA*, 20, 167

- Giles, H. A. C., Collier Cameron, A., & Haywood, R. D. 2017, *MNRAS*, **472**, 1618
- Goodman, J., & Weare, J. 2010, *Communications in Applied Mathematics and Computational Science*, **5**, 65
- Helminiak, K. G., Ukita, N., Kambe, E., et al. 2017, *MNRAS*, **468**, 1726
- Hilditch, R. W. 2001, *An Introduction to Close Binary Stars* (Cambridge: Cambridge Univ. Press)
- Hu, K., Yu, Y.-X., Zhang, J.-F., & Xiang, F.-Y. 2020, *AJ*, **160**, 62
- Huang, Y., Liu, X. W., Chen, B. Q., et al. 2018, *AJ*, **156**, 90
- Kirk, B., Conroy, K., Prša, A., et al. 2016, *AJ*, **151**, 68
- Li, C.-q., Shi, J.-r., Yan, H.-l., et al. 2021, *ApJS*, **256**, 31
- Liu, N., Fu, J.-N., Zong, W., et al. 2019, *RAA*, **19**, 075
- Lu, H.-p., Zhang, L.-y., Michel, R., & Han, X. L. 2020, *ApJ*, **901**, 169
- Lucy, L. B. 1967, *ZAp*, **65**, 89
- Lurie, J. C., Vyhmeister, K., Hawley, S. L., et al. 2017, *AJ*, **154**, 250
- McIntosh, S. W., Leamon, R. J., Krista, L. D., et al. 2015, *NatCo*, **6**, 6491
- McQuillan, A., Aigrain, S., & Mazeh, T. 2013, *MNRAS*, **432**, 1203
- McQuillan, A., Mazeh, T., & Aigrain, S. 2014, *ApJS*, **211**, 24
- Meng, G., Zhang, L.-Y., Pi, Q.-F., et al. 2021, *RAA*, **21**, 115
- Montet, B. T., Tovar, G., & Foreman-Mackey, D. 2017, *ApJ*, **851**, 116
- Morris, B. M., Davenport, J. R. A., Giles, H. A. C., et al. 2019, *MNRAS*, **484**, 3244
- Niu, H.-B., Fu, J.-N., Wang, J.-X., & Li, C.-Q. 2022, *RAA*, **22**, 015016
- Pan, Y., Fu, J.-N., Zong, W., et al. 2020, *ApJ*, **905**, 67
- Pi, Q.-f., Zhang, L.-y., Bi, S.-l., et al. 2019, *ApJ*, **877**, 75
- Prša, A., Batalha, N., Slawson, R. W., et al. 2011, *AJ*, **141**, 83
- Prša, A., & Zwitter, T. 2005, *ApJ*, **628**, 426
- Rappaport, S., Deck, K., Levine, A., et al. 2013, *ApJ*, **768**, 33
- Reinhold, T., Cameron, R. H., & Gizon, L. 2017, *A&A*, **603**, A52
- Reinhold, T., Reiners, A., & Basri, G. 2013, *A&A*, **560**, A4
- Ruciński, S. M. 1969, *AcA*, **19**, 245
- Slawson, R. W., Prša, A., Welsh, W. F., et al. 2011, *AJ*, **142**, 160
- Solanki, S. K. 2003, *A&ARv*, **11**, 153
- Toonen, S., Portegies Zwart, S., Hamers, A. S., & Bandopadhyay, D. 2020, *A&A*, **640**, A16
- van Hamme, W. 1993, *AJ*, **106**, 2096
- Wang, J., Fu, J., Zong, W., et al. 2022, *MNRAS*, **511**, 2285
- Wilson, R. E. 1979, *ApJ*, **234**, 1054
- Wilson, R. E. 1990, *ApJ*, **356**, 613
- Wilson, R. E. 2012, *AJ*, **144**, 73
- Wilson, R. E., & Devinney, E. J. 1971, *ApJ*, **166**, 605
- Zhang, B., Li, J., Yang, F., et al. 2021a, *ApJS*, **256**, 14
- Zhang, L.-Y., Long, L., Shi, J., et al. 2020, *MNRAS*, **495**, 1252
- Zhang, L.-y., Meng, G., Long, L., et al. 2021b, *ApJS*, **253**, 19
- Zhu, Z.-Z., Zhang, L.-Y., Meng, G., et al. 2021, *RAA*, **21**, 084
- Zong, W., Charpinet, S., Fu, J.-N., et al. 2018a, *ApJ*, **853**, 98
- Zong, W., Fu, J.-N., De Cat, P., et al. 2018b, *ApJS*, **238**, 30
- Zong, W., Fu, J.-N., De Cat, P., et al. 2020, *ApJS*, **251**, 15